PHYSICAL REVIEW B VOLUME 29, NUMBER 3 1 FEBRUARY 1984

Nuclear-magnetic-resonance study of methane adsorbed on graphite

Jeffrey H. Quateman* and Michael Bretz
Department of Physics, University of Michigan, Ann Arbor, Michigan 48109
(Received 11 May 1983)

We have measured the spin-spin (T_2) and spin-lattice (T_1) relaxation times of methane adsorbed on Grafoil using pulsed nuclear-magnetic-resonance techniques. Data were taken between 45 and 105 K and between 0.20 and 1.1 monolayers at frequencies of 4.586 and 2.107 MHz. In addition, proton relaxation times were measured with mixtures of 50% CD_4+50% CH_4. It was determined that relaxation was via intramolecular dipolar interactions. Activation energies computed from the T_1 data provide evidence for both coverage-driven (at 0.87 monolayers) and temperature-driven commensurate-incommensurate phase transitions. A frequency-independent jump in T_1 at lower coverages indicates first-order melting to the liquid at approximately 57 K. Higher-temperature data find supporting evidence for a hypercritical fluid (two-dimensional gas) above a critical temperature of about 75 K.

I. INTRODUCTION TO METHANE MONOLAYERS

The considerable interest in adsorbed films research on graphite is sustained by a continual unfolding of novel observations and predictions. Much of the field's richness arises from the interplay between interparticle interactions and substrate well geometry. For methane, the lattice parameter of the bulk solid closely matches graphite's basal plane mosaic. Tessier and Larher[1] report a dimensional incompatibility of only 1.7% at the triple-point temperature for methane compared to 4.6% for krypton and −3.5% for xenon, whose large hard core prevents registry with the graphite at any temperature. We expect a registered methane phase to exist at low T, but it should be disrupted by thermal expansion as temperature rises.

In this paper we report on NMR dynamics associated with phase transitions occurring in the methane monolayer between 45 and 110 K. Although a low-temperature (less than 30 K) NMR exploration of rotational ordering would also be appropriate, this is left for a later study. Before discussing our own work we review previous neutron scattering, heat capacity, and NMR measurements of methane adsorbed on graphite. Section II contains an outline of NMR theory while the spectrometer and data-acquisition procedures are explained in Sec. III. We present our results sequentially with coverage in Sec. IV, leaving a quantitative analysis of the T_1 minimum for Sec. V.

A neutron scattering survey of monolayer methane adsorbed on Grafoil has recently been made by Vora, Sinha, and Crawford.[2] Their resulting phase diagram is given in Fig. 1. A $\sqrt{3}\times\sqrt{3}R\,30^\circ$ registered phase was observed to coexist with a two-dimensional (2D) fluid for partial CD_4 monolayers below 50 K. In a narrow temperature range above 50 K they find an ($\lesssim 1\%$) expanded solid and fluid phase with probable first-order melting at 60 K. Near monolayer completion the commensurate phase occupies the entire surface but gives way to a compressed solid phase through a commensurate-incommensurate transition (CIT) at still higher coverages. They report that the CIT is continuous with possible formation of defect regions or microdomains and that the compressed solid melts continuously to the fluid near 100 K. Fluidlike scattering peaks were seen at high temperatures and densities but could not be further specified as liquids or gases. It is stressed that 2D methane has the unusual property of always melting from the incommensurate phase.

This work has been extended to include a detailed line-shape analysis of the 2D incommensurate solid-fluid transition,[3] which shows substantial thermal diffuse scattering. A structure-factor analysis of the 2D incommensurate solid was also performed,[4] and phonon scattering information was obtained.

A careful neutron scattering examination of CD_4 triple-point melting at 0.6 layers by Glachant, Coulomb, Bienfait, and Dash[5] showed an abrupt drop in the film

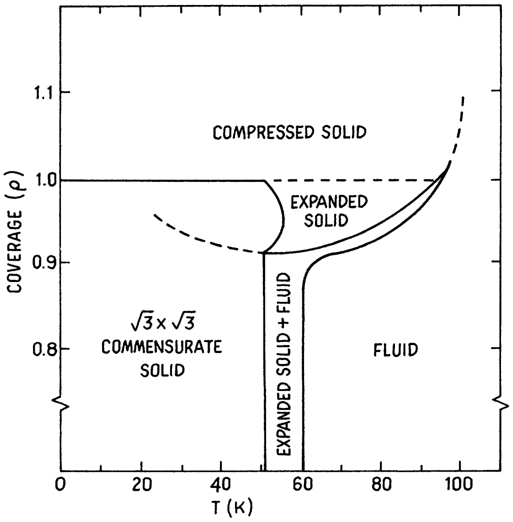

FIG. 1. Methane phase diagram from neutron scattering.

spatial correlation range from 230 to 30 Å at 56±0.4 K. This is clear-cut evidence for first-order melting. Quasielastic neutron scattering (QENS) was used by Coulomb, Bienfait, and Thorel[6] to explore the fluid mobility. They observe strong variations versus coverage for CH_4 at 90 K which is in the "hypercritical fluid" regime (a compressible 2D fluid above its critical point). Subsequently, Coulomb *et al.*[6] distinguished between 2D fluid and hypercritical fluid near the 2D critical point at 75 K (as determined by Thomy and Duval[7]) and estimated activation energies for diffusion. They also found the expanded solid phase above 47–50 K and report that it probably converts to the low-temperature ordered solid via a continuous transition. A QENS study of methane rotational diffusion[8] concludes that the motion of CH_4 molecules is isotropic at 55 K for 0.63 and 0.90 layers while Newbery *et al.*[9] explore rotational tunneling effects at much lower temperatures (below 30 K).

Heat-capacity measurements were made recently for CH_4 monolayers on Grafoil by Marx and Wasserman.[10] They see a broad, weak anomaly at 47.6 K and a strong, narrow peak at 56.35 K for coverages below 0.8 layer, which correspond to the registered solid-expanded solid and expanded solid-fluid transitions, respectively. Also, a rise in the triple-point temperature by a few degrees is noted between 0.7 and 0.8 layers. At lower temperatures (30 K) Migone, Chan, and Boyer[11] see a rotational heat-capacity peak.

An extensive NMR exploration of CH_4 monolayers on Spheron 6, a graphitized carbon black, was performed some time ago by Riehl and Koch.[12] They measured both spin-lattice (T_1) and spin-spin (T_2) relaxation times at 30 MHz for 0.02 to 0.8 layers between 4 and 100 K. A discontinuity in T_2 was observed near the triple line and two T_1 minima were found, from which activation energies were obtained. Later understanding of the surface heterogeneity of Spheron 6 and of T_2 shortening in 2D systems[13] has superseded their conclusions regarding interaction mechanisms, oriented gases, and deuteration effects. The present NMR experiment has repeated much of the Riehl and Koch work, but with the superior substrate, Grafoil. We also operate at a much lower frequency, 4.586 MHz, which minimized rf heating. Our signal-to-noise ratio is much improved over their measurements, which allows the observation of features missed previously. Furthermore, we take considerable data above 0.8 layers, where important phase dynamics occur. For a preliminary report of our findings see Quateman and Bretz.[14]

II. NUCLEAR-MAGNETIC-RESONANCE THEORY

A. Three-dimensional versus 2D relaxation theory

Nuclear magnetic resonance (NMR) is used to explore the microscopic environment of solids, liquids, and gases where a collection of spins is in thermal equilibrium with a lattice. The Bloch equations in the absence of a driving force,

$$\frac{dM_z}{dt}=\frac{M_0-M_z}{T_1}\,,$$

$$\frac{dM_x}{dt}=\frac{-M_x}{T_2}\,,$$

$$\frac{dM_y}{dt}=\frac{-M_y}{T_2}\,,$$

describe the usual experimentally observed exponential decay of the magnetization components M_x,M_y,M_z when disrupted from their static equilibrium positions $M_z=M_0$ and $M_x=M_y=0$. Mechanisms for effecting this decay are static and dynamic local magnetic fields and gradients arising from magnetic dipolar interactions between molecules and from the anisotropic diamagnetism of graphite (see Farrar and Becker[15] for other relaxation mechanisms and pulsed NMR techniques for measuring T_1 and T_2).

A theory to compute T_1 (longitudinal) and T_2 (transverse) relaxation times in three dimensions (3D) has been developed with the use of the techniques of density-matrix perturbation theory. The T_1 result is[16]

$$\frac{1}{T_1}=\tfrac{3}{2}\gamma^4\hbar^2 I(I+1)[J_1(\omega_L)+J_2(2\omega_L)] \tag{2.1}$$

for a pair of nuclear spins I having a magnetogyric ratio γ and precessing at the Larmor frequency ω_L in the applied magnetic field B_0.

The spectral density function $J_k(\omega)$, is the time Fourier transform of $G(\tau)$

$$J_k(\omega)=\int_{-\infty}^{\infty} G_{kk}(\tau)e^{-i\omega\tau}d\tau\,,$$

where the correlation function

$$G_{mn}(\tau)=[\langle m\,|\mathcal{H}_1(t-\tau\,|\,n\rangle\langle n\,|\mathcal{H}_1(t)\,|\,m\rangle]_{\rm av}$$

defines a time scale τ associated with the system at hand whose time-dependent Hamiltonian is $\mathcal{H}_1(t)$. The motion stays correlated over a time τ_c given by

$$\tau_c\sim\frac{1}{G_{mn}(0)}\int_0^{\infty} G_{mn}(\tau)d\tau\,.$$

The same method can be applied to the x component of the magnetization giving

$$\frac{1}{T_2}=\gamma^4\hbar^2 I(I+1)[\tfrac{3}{8}J_0(0)+\tfrac{15}{4}J_1(\omega_L)+\tfrac{3}{8}J_2(2\omega_L)]\,. \tag{2.2}$$

Note that it is motion at zero frequency ω (static local fields), as well as at the Larmor frequency that determines T_2. T_1 is only affected by motion that has Fourier components at the Larmor frequency. If the correlation time is very short compared to the Larmor frequency (as in liquids), then the spectral density function $J(\omega)$ at $\omega=\omega_L$ equals $J(0)$ and $T_1=T_2$. Although it is not evident from the above discussion, this approach assumes that the correlation function $G(\tau)$ decays faster than T_2. The constraint is implicit in the time-dependent perturbation theory, which was used to solve the equations of motion of the density matrix.

To avoid this restriction the problem can be approached using techniques developed by Kubo.[17] Instead of calculating $d\vec{M}/dt$ using perturbation theory, the Kubo method starts with the theoretical expressions for the transverse (T_2) and longitudinal (T_1) relaxation functions,[18]

$$F(t)=\exp(-i\omega_L t)\mathrm{Tr}[I_+(t)I_-(0)]/\mathrm{Tr}[I_+I_-]\ ,$$

$$L(t)=\mathrm{Tr}[I_z(0)I_z(t)]/\mathrm{Tr}[I_z^2]\ ,$$

respectively. I_α ($\alpha=+,-,z$) is the spin operator for the total system and

$$I_\alpha(t)=\exp(i\mathscr{H}t)I_\alpha\exp(-i\mathscr{H}t)\ .$$

These functions are expanded in powers of $\mathscr{H}$. For long times, however, any truncated expansion diverges. Kubo overcame this by expanding the logarithm of the relaxation function to an order n. This is equivalent to an infinite-order power-series expansion, where the first n terms are exact and higher-order terms are approximate.[13]

Kubo's results to second order, called the cumulant expansion, are

$$F(t)=\exp\left[-\int_0^t(t-\tau)\sum_{m=-2}^{+2}\left[3-\frac{m^2}{2}\right]G_m(\tau)\times\exp(im\omega_0 t)d\tau\right]\ ,$$

$$L(t)=\exp\left[-\int_0^t(t-\tau)\sum_{m=-2}^{+2}m^2G_m(\tau)\exp(im\omega_0 t)d\tau\right]\ .$$

If the correlation function decays sufficiently fast, the integrals can be extended to infinity and then

$$L(t)\sim\exp(-t/T_1)\ ,$$

$$F(t)\sim\exp(-t/T_2)\ ,$$

where

$$1/T_1=\gamma^4\hbar^2[J_1(\omega_L)+4J_2(2\omega_L)]$$

and

$$1/T_2=\gamma^4\hbar^2[\tfrac{3}{2}J_0(0)+J_1(\omega_L)+\tfrac{3}{2}(2\omega_L)]$$

are results we have seen using density-matrix techniques. In three-dimensional systems the assumption is valid.

However, in two dimensions, where the motion is confined to a plane, there is an anisotropy of the intermolecular magnetic dipolar interaction which does not easily average away. A long tail results in the $m=0$ autocorrelation function $G_0(\tau)$, so the integral in $F(t)$ cannot be extended to infinity. In effect, this shortens T_2 so that in the motional narrowing limit ($\omega\tau_c \ll 1$) T_2 is not equal to T_1, but substantially less. For longitudinal (T_1) relaxation the $m=0$ term disappears and the integrals can be extended to infinity (since the $m\neq 0$ terms oscillate rapidly).

Cowan[13] has formulated the theory and calculated correlation functions and relaxation times for *inter*molecular dipolar relaxation. Although the solutions cannot be described in closed form, the relaxation dependence on correlation times is that for 3D. The effect of reduced dimensionality on *intra*molecular interactions has not been studied.

B. Dipolar relaxation in solids, liquids, and gases

When the motion of a molecule in diatomic liquids and solids undergoing *intra*molecular relaxation can be described by a diffusion equation

$$\frac{\partial P}{\partial t}=\frac{D}{a^2}\nabla^2 P$$

[where $P(r,t)$ is the probability of finding the spin-spin axis in a direction Ω at a time t, and where ∇^2 is the Laplacian operator on the surface of a sphere], we can integrate the appropriate expression for the correlation function $G_m(t)$ over all possible Ω's (Ref. 16, p. 298) to give

$$\left[\frac{1}{T_1}\right]_{\mathrm{intra}}=\frac{2}{5}\frac{\gamma^4\hbar^2}{b^6}I(I+1)\left[\frac{\tau_c}{1+\omega^2\tau_c^2}+\frac{4\tau_c}{1+4\omega^2\tau_c^2}\right]\ . \tag{2.3}$$

If the diffusion coefficient can be simply related to τ_c by $D=a^2/6\tau_c$ (a is a hard-core dimension, not necessarily the hard-core radius of the molecule), then for liquids where $\omega\tau_c \ll 1$

$$\left[\frac{1}{T_1}\right]_{\mathrm{intra}}=\frac{\gamma^4\hbar^2}{b^6}\frac{a^2}{D}\ . \tag{2.4}$$

Similarly,

$$\frac{1}{T_2}=\frac{1}{5}\frac{\gamma^4\hbar^2}{b^6}I(I+1)\left[3\tau_c+\frac{5\tau_c}{1+\omega^2\tau_c^2}+\frac{2\tau_c}{1+4\omega^2\tau_c^2}\right]\ , \tag{2.5}$$

valid only for $\tau_c \ll T_2$.

For *inter*molecular relaxation in a liquid we compute $G_m(t)$ by integrating, not over axes of rotation, but over the intermolecular distance r (with initial condition $r=r_0$). In this case

$$P(r,r_0,t)=(8\pi Dt)^{-3/2}\exp\left[-\frac{(r-r_0)^2}{8Dt}\right]$$

giving

$$\left[\frac{1}{T_1}\right]_{\mathrm{inter}}=\frac{\pi}{5}\rho\frac{\gamma^4\hbar^2}{bD} \tag{2.6}$$

(for 3D liquids). The main difference between intramolecular and intermolecular relaxation in liquids is the appearance of the density of spins ρ in Eq. (2.6).

The relative contributions of the intramolecular and intermolecular relaxation in T_1 can be estimated from Eqs. (2.4) and (2.6). For two-dimensional systems ρ must be suitably modified to account for the change in dimensionality from (length)^3 to (length)^2. We have

$$\left[\frac{1}{T_1}\right]_{\mathrm{inter}}\Big/\left[\frac{1}{T_1}\right]_{\mathrm{intra}}\cong\rho\frac{b^6}{a^4}\ ,$$

where $b = 1.78\times 10^{-8}$ cm.[19] If we assume close-pack spacing which has the largest ρ, then $a = 4.129\times 10^{-8}$ cm and $\rho \cong 5.8\times 10^{14}/\text{cm}^2$, giving

$$\left[\frac{1}{T_1}\right]_{\text{inter}} \Big/ \left[\frac{1}{T_1}\right]_{\text{intra}} \cong 0.02 \; .$$

This implies that methane dipolar relaxation contributions to T_1 should be dominated by intramolecular interactions.

For a solid relaxing via intermolecular dipolar processes, the diffusion coefficient D is equal to $l^2/6\tau_c$, where l is the nearest-neighbor distance in a lattice. We have

$$\left[\frac{1}{T_1}\right]_{\text{inter}} = \frac{8\pi}{5}\gamma^4\hbar^2 I(I+1)\frac{1}{l^6}\Phi(\tau_c) \; , \qquad (2.7)$$

where $\Phi(\tau_c)$, a function of the correlation time, depends on the particular lattice but resembles Eq. (2.5) (for intramolecular relaxation).[20] The salient feature here is the $1/l^6$ or ρ^2 (ρ^3 in 2D) dependence of $1/T_1$ for intermolecular relaxation in solids. For intramolecular relaxation there is no such density dependence.

In a polyatomic gas, dipolar relaxation is intramolecular. In particular, the dipolar coupling to a nucleus depends on its axis of rotation $\vec{J}$ which changes only during a collision. The analysis is similar to that for liquids and results in Ref. 16 (p. 319),

$$1/T_1 \sim \tau_c$$

where τ_c is the time a molecule stays in a particular rotation state $\vec{J}$ or the time between collisions. From elementary kinetic theory

$$\tau_c \sim 1/\sqrt{T}$$

and

$$1/\tau_c \sim \rho \; ,$$

so

$$T_1 \sim \sqrt{T}\rho \; .$$

This is the signature of a polyatomic gas (e.g., methane).

For comparison, a monoatomic gas (which cannot have intramolecular magnetic fields) experiences a local field only during a collision. At other times there are no nuclei close enough to perturb it. Transition proabilities are proportional to the collision frequency $1/\tau_c$ and

$$\frac{1}{T_1} \sim \frac{1}{T_c}$$

or

$$T_1 \sim \frac{1}{\sqrt{T}\rho}$$

which is the inverse dependence on T and ρ from that of a polyatomic gas. (Note: $T_1 \sim \tau_c$ should not be confused with the regime in a solid where $\omega\tau_c \gg 1$ and $T_1 \sim \omega^2\tau_c$.)

III. THE APPARATUS AND DATA COLLECTION

A. The pulsed NMR spectrometer

The spectrometer is a standard phase-coherent machine (see Ref. 15, for example) with the notable addition of computer control and data collection. We used a Cormemco Z-2D microcomputer, a Z-80 based machine, to create pulse sequences and gate them to the transmitter, to collect and signal average the resultant echos, to determine echo heights, and to compute relaxation times. The spectrometer operated between 2 and 20 MHz (limited by transmitter gain) with a transmitter power of 1 kW and a receiver noise voltage of 1.9 V/$\sqrt{\text{Hz}}$ with a bandwidth of 13 MHz. A block diagram of the spectrometer is provided in Fig. 2. Further design details can be found in Ref. 21.

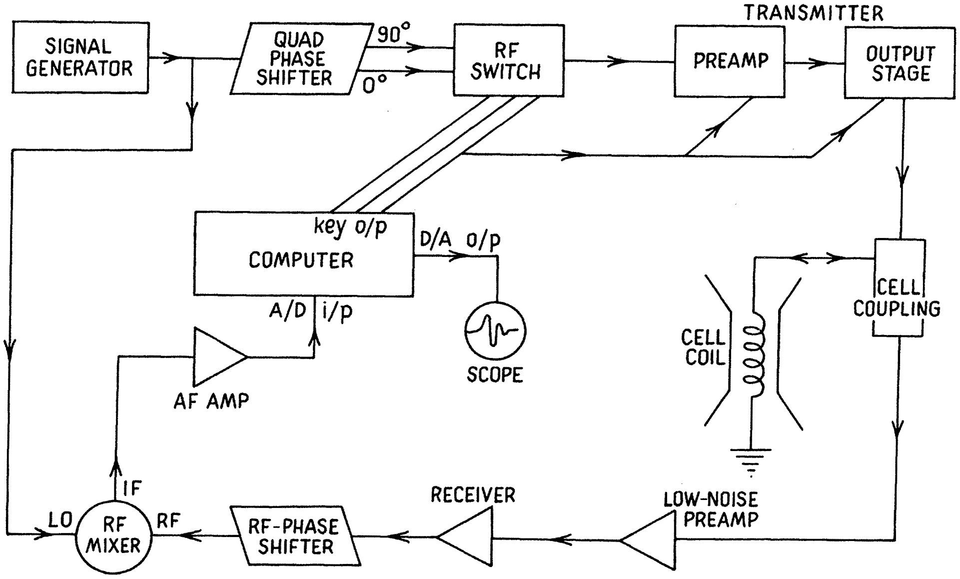

FIG. 2. NMR spectrometer block diagram.

The cell coil coupling circuit[22] is shown in Fig. 3. To minimize the recovery time of the receiver, two crossed diodes (D_3 and D_4) are placed before the receiver preamp. These limit the voltage across the preamp input to ± 0.7 volts. To ensure that the transmitter current flows into the NMR cell coil L_2 and not into the diodes, a second inductance, L_3, is placed in the circuit. This acts as an rf choke and directs the current to the low-impedance series circuit L_2C_2. The high-input impedance of the field-effect transistor (FET) preamp prevents a voltage drop across L_3 when detecting a signal. The receiver still must recover from the ± 0.7-V overload to the point where it is sensitive to microvolts.

The shortest T_2 measurable is limited by the recovery time of the receiver after an rf pulse, which is mainly the ring-down time of the sample coil rather than the slew time of the receiver. In this experiment a recovery time of 300 μsec limited T_2 measurements to greater than 800 μsec. Resistor R_1 and crossed diodes D_1 and D_2 give fast rise and fall times of the rf-pulse envelope and decouple the transmitter circuit from the receiver circuit once the pulse has finished.

The signal-to-noise ratio of the receiver circuit is[22]

$$\frac{S}{N}=\frac{f}{2}\left[\frac{1}{J}\right]^{1/2}\left[(\chi_0 Q_2)\left[\frac{\chi_0 B_0^2 V}{kT_R}\right]\times\left[\frac{\omega_L}{\Delta\omega}\right]\left[1+0.9\frac{a}{b}\right]\right]^{1/2},$$

where χ_0 is the magnetic susceptibility of the sample, T_R is room temperature (environment of the circuitry), Q_2 is the quality factor of the sample coil with radius a and length b, and $\Delta\omega$ is the bandwidth of the receiver. The J takes into account additional noise due to the circuit and is used to determine L_3.

B. The sample cell

The sample cell was designed to optimize the rf magnetic field B_1 and the signal-to-noise ratio S/N, while keeping B_0 and B_1 as homogeneous as possible.[15] The transmitter requirements imply a small cell volume since $B_1 \sim \sqrt{L2/V}$, but since $S/N \sim \sqrt{V}$, a compromise was reached. Because most of the volume of the cell was graphite the filling factor was necessarily small (~ 0.5) which necessitated a large cell coil. However, this was detrimental to both the homogeneity of B_0 and B_1 and the strength of B_1. (These systematics are described carefully in the next section.) In addition, the rf pulse sent to the cell induces eddy currents in the graphite, heating the sample. The power in the coil and hence the eddy currents is proportional to the frequency squared. The frequency was kept low (2.107 and 4.586 MHz) to minimize this inductive heating. In addition sheets of 1-mil Mylar were placed between the Grafoil layers to further reduce eddy currents.

The sample cell was machined out of a cured Stycast 1266 epoxy block and consisted of a thin-walled cylindrical tube of inside diameter $1\frac{1}{4}$ in. and length $1\frac{1}{2}$ in. with a poured bottom and a separate machined top with a stainless-steel fill line epoxied in place. Threads at 36 per inch were cut into the outside of the cell as a form for the NMR coil. The empty cell and top were pumped on by a mechanical pump for 24 h to complete the curing.

Approximately 19 g of Grafoil (Union Carbide) were cut into rectangular sheets of decreasing widths, fitted snugly in the Stycast cell [Fig. 3(a)], then baked for 24 h at 1000 °C under a vacuum of 10^{-5} Torr to remove any oils and other contaminants received during manufacturing and handling. The Grafoil was transferred to the cell under a dry-N_2 atmosphere and stacked alternately with the 1-mil Mylar sheets. The dead volume of the cell was 19 cm^3. The cell was attached to the bottom platform with the Grafoil sheets perpendicular to $\vec{B}_0$ (see Fig. 3). A 25-mil i.d. stainless-steel fill line ran up a vacuum shroud to the top of the insert. The shroud thermally isolated the fill line from the bath and prevented the methane from condensing in the fill line.

The coil consisted of 58 turns of no. 24 copper wire wound on the threads cut in the cell and then epoxied in place. The rigidity of the coil reduced the possibility of microphonics. The coil inductance was approximately 74 μH and it had a Q of 50 at 4.5 MHz with the Grafoil in place. The signal-to-noise ratio for 1 monolayer coverage was 5, while the calculated S/N for a filling factor of 1 at a cell temperature of 77 K was 10. The S/N decreased linearly with decreasing coverage.

C. The magnet

The magnet used in the experiment was a Varian 12-in. research magnet with the pole caps removed to permit a

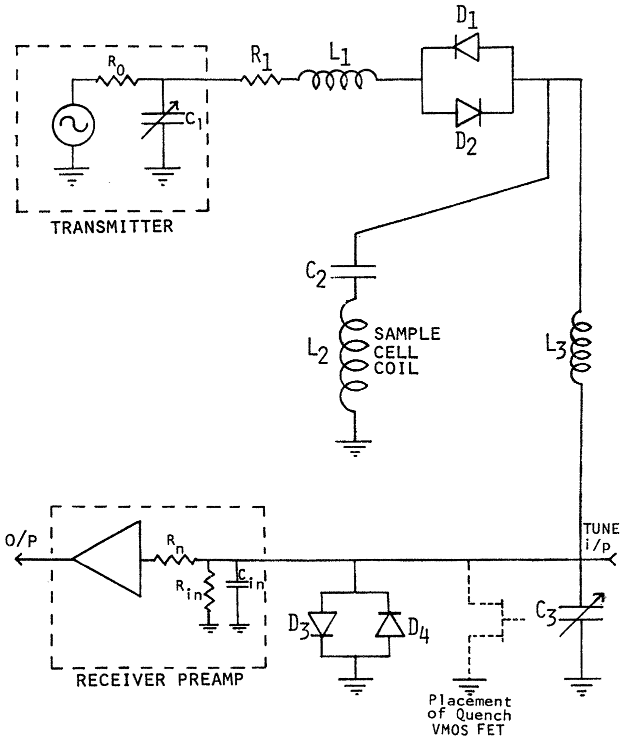

FIG. 3. Cell coil coupling circuit.

glass Dewar system to fit between the poles. Fields up to 2 kG could be obtained with the 5-in. gap.

D. Cryostat and temperature control

For the methane experiments the temperature needed to be regulated from 40 to 110 K. To this end a cryostat insert was designed to raise temperatures above that of the cryogenic bath [Fig. 4(a)]. It consisted of two copper platforms connected to each other by thin-walled stainless-steel tubing. This provided weak thermal links between the platforms and the bath. The temperature of each platform was controlled separately by using two ac wheatstone-bridge temperature controllers based on a circuit of Rochlin.[23] Thermometers were $\frac{1}{8}$-W Allen-Bradley carbon composition resistors in a three-wire configuration, and the heaters consisted of 100 Ω of 2-mil Evanohm wire.

Stycast is a poor thermal conductor. To ensure accurate temperature measurement the cell had two well-separated thermometers embedded in it: a calibrated germanium resistance thermometer (GRT) from Scientific Instruments (Model 3) and a platinum resistance thermometer (PLT) model No. PT-103 from Lake Shore Cryotronics, Inc. Both resistances were measured by a four-lead dc hook up and were used over the entire temperature range 45—105 K. Temperature conversion was via least-square fits to third-order Chebychev polynomials, giving temperature errors of about 1%. Stability and repeatability were less than 0.5% to within the resolution of the measuring circuit ($\Delta R/R < 0.1\%$). The small static magnetic field B_0 (<2 kG) did not affect either thermometer to within our measurement resolution.

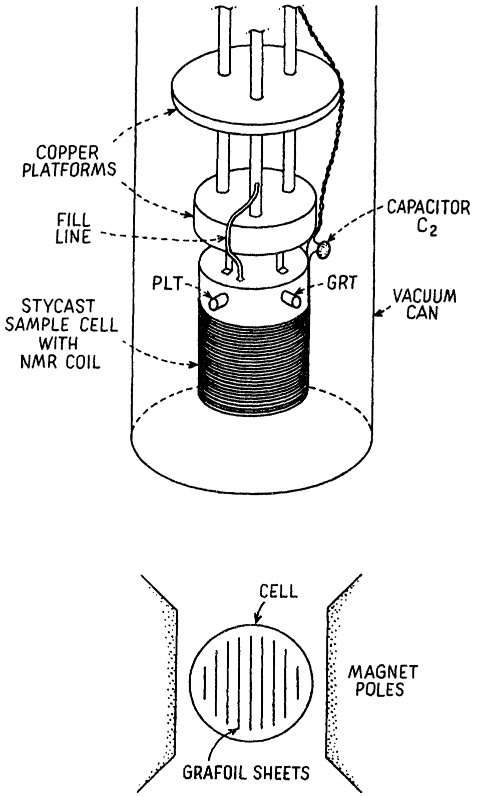

FIG. 4. (a) Sketch of cryostat insert and cell. (b) Orientation of Grafoil in B_0.

E. Gas-handling system

Known quantities of ultra-high-purity CH_4 (Matheson Co.), CD_4, and He gas were allowed into the cell via a gas manifold consisting of a 26-cm^3 calibrated volume, a 1000-Torr Baratron capacitance manometer, and associated plumbing.

F. Adsorption isotherm

Figure 5 shows a stepwise CH_4 adsorption isotherm taken at 77 K. The presence of steps reflects the successive buildup of discrete monolayers on a homogeneous surface,[24] confirming that the Grafoil adsorption surface has been adequately cleaned and protected. For comparison of our NMR results with the neutron scattering study of Vora *et al.*,[2] we took their criterion of monolayer completion as the inflection point along the first step of the isotherm. This was determined to be 93.3 cm^3 at STP from a plot of isotherm slopes $\Delta N_{ad}/\Delta P$ plotted versus total gas adsorption N_{ad} in the Fig. 5 inset. We note that Thomy and Duval[7] use a different criterion for monolayer completion, which is better and probably a few percent lower in coverage than our determination.

Gas was metered with 0.1% accuracy into the cell over

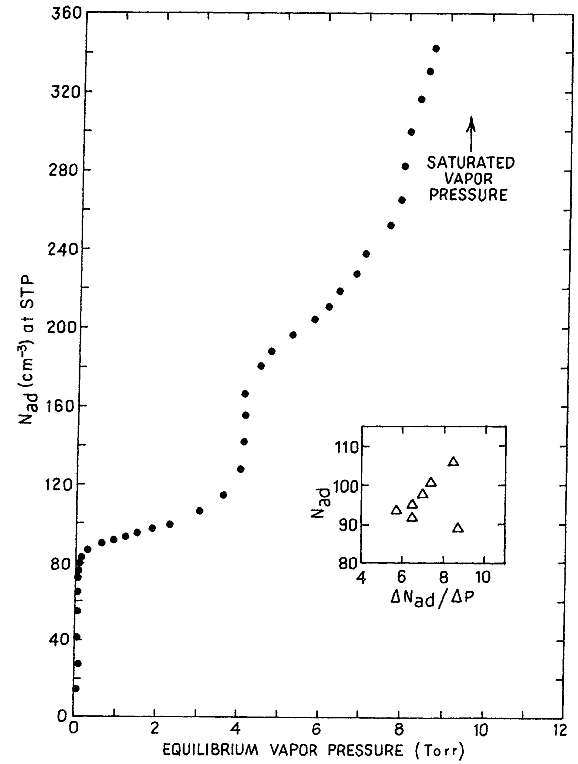

FIG. 5. A 77.3-K methane isotherm. Inset: isotherm slope vs coverage.

a period of $\frac{1}{2}$ to 1 h. A small quantity of ^{4}He gas, 0.072 cm^3 at STP, was then admitted into the cell. The helium provided a 0.5-Torr vapor pressure (at 50 K), ensuring thermal equilibrium between all areas of the sample. (Both the Stycast and Grafoil have poor thermal conductivity.) At the temperatures of our experiment (45 K or more), negligible ^{4}He gas is adsorbed on the graphite. The methane film was annealed by raising the temperature of the cell to 110 K (where there is a CH_4 vapor pressure) for 6 h and then slowly lowering it to 77 K over another 12-h period. To obtain temperatures of less than 77 K the liquid-nitrogen bath was pumped (obtaining 50 K) or a liquid-helium bath was used. In either case the temperature was lowered to a minimum of 40 K over another 4-h time span. The vapor pressure of the methane film was measured (without the ^{4}He) at 105 K for coverages up to 0.90 monolayers. But since less than 0.1% of the total gas admitted appear in the 3D vapor phase, no coverage correction was made for desorption.

G. Relaxation-time systematics

Spin-spin relaxation times T_2 were measured using a standard Meiboom-Gill sequence with a $\pi/2$ pulse being 15 μsec (Ref. 15). The inhomogeneity of the static magnetic field, B_0, and the magnetic field gradients caused by the diamagnetism of the graphite itself limited the apparent free-induction decay rate T_2^* to 0.5 msec, independent of temperature and coverage. The sample coil was necessarily large, giving an inhomogeneity to the rotating magnetic field B_1, which manifests itself by an incorrect rotation for some nuclei in the sample. The resulting incomplete 90° or 180° rotations of $\vec{M}_0$ show up by all odd-numbered echos being slightly smaller than even-numbered ones. The problem was avoided by using only even-numbered echo heights for determining T_2. Echo heights were determined by using the points of the second echo as an "analytical function" with subsequent even echos fit to this "function" with a one-parameter (height) linear least-squares analysis and then fit to an exponential decay.

Spin-lattice relaxation times T_1 were measured using 180°,τ,90°,τ',180° pulse sequences (where $\tau' \ll T_1$) rather than the standard 180°,τ,90° sequences, which look at the amplitude of the free-induction decay. Owing to the long receiver recovery time and the short T_2^*, it was necessary to create an echo and plot its height versus τ to determine T_1. All T_1 decays were exponential over the decade and a half of echo heights. An example is shown in Fig. 6. They were reproducible to within 5% from day to day and also from run to run after thermal cycling of the cell and removal and subsequent replacement of the methane gas. T_2 data were reproducible to within 10%.

The T_2 decays, however, had two systematics present. The first systematic occurred in the Meiboom-Gill sequence when the time 2τ between 180° pulses was long (greater than 2 msec). There the echo amplitude initially fell faster than exponentially, becoming exponential after 2 or 3 echos. As τ was shortened the effect decreased and eventually disappeared, giving only the previous exponential decay (see Fig. 6). Decreasing τ in a Meiboom-Gill sequence does correct for the long-time nonexponential $\exp(-t^3)$ decay of molecules diffusing in a magnetic field gradient.[15] To explain our short-time phenomenon, consider that Grafoil possesses a distribution of graphite crystallite sizes. Owing to the diamagnetic nature of the graphite, there are strong magnetic field gradients at the crystallite boundaries where step dislocations are present, crystallites meet, etc. If the methane molecules diffuse on the surface without encountering many boundaries (i.e., large crystallites), then T_2 decays exponentially. For small crystallites, however, molecules will diffuse to the boundaries, sense field gradients, and enhance the T_2 decay. For a distribution of crystallite sizes the initial echo amamplitude will fall rapidly as the molecules on the smaller crystallites dephase, leaving only the molecules on larger crystallites whose signal decays exponentially. Decreasing τ corrects for this fall off on the small crystallites and gives an exponential decay for T_2.

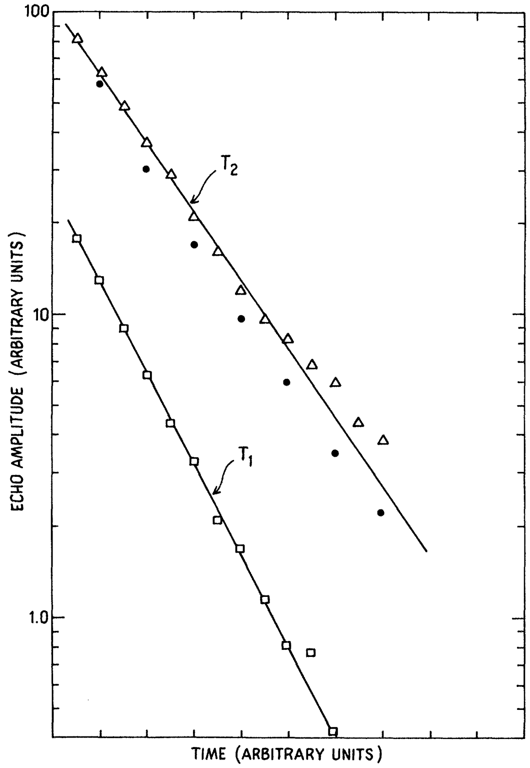

FIG. 6. Representative T_1 and T_2 decays.

The second T_2 systematic is believed to be a deficiency in phase cancellation of the Meiboom-Gill sequence.[25] The T_2 decays level off for long times if τ is kept short. This "base-line effect" decreased with increasing τ and was only noticeable for T_2's greater than 5 msec. We overcame these problems by taking two T_2 measurements, one with a short $\tau \leq 1$ msec (to correct for the diffusion effect), and one with a long τ. T_2's were calculated from both measurements (ignoring data points affected by the systematics) and compared for consistency. This proved satisfactory.

Other systematic investigations were performed on the system. T_1 and T_2 decays were measured both on and off resonance (up to 3 KHz) by both varying B_0 and ω_0. No effect on relaxation times was observed. The Stycast sample cell, as well as the Mylar insulating sheets, contain hydrogen nuclei (protons). As expected, no NMR signal was seen at any temperature from these nuclei because dipolar broadening of solids limits T_2 to microseconds.

Friedman, Mellet, and Richardson[26] noted dipolar couplings between ^{3}He and ^{19}F nuclei for ^{3}He adsorbed on fluorocarbon beads. They found that the ^{3}He T_1 decay was dominated by the coupling to the ^{19}F spin system. In the present experiment all but a small fraction of the methane was adsorbed on ^{12}C atoms, which have no nuclear dipole moments. If there was, nevertheless, strong coupling between the two systems, one might expect the CH_4 polarization to be pumped by the Stycast as in the Friedman experiment (since $\omega\tau_c \gg 1$, T_1 of the Stycast is very long). The rich temperature and coverage variations of T_1 suggest otherwise.

IV. RESULTS AND INTERPRETATIONS

The 4.586-MHz T_1 and T_2 measurements are presented and discussed in sequentially increasing coverage groups of 0.2, 0.4—0.75, 0.80—0.85, and 0.88—1.03 monolayers. A phase diagram is constructed, mostly from the T_1 data, and compared to the previous neutron scattering work. Then, data obtained for a 50% mixture of $CH_4 + CD_4$ and for pure CH_4 at 2.107 MHz are given for coverages between 0.70 and 0.94 monolayers. These provide consistency checks to our phase-diagram interpretations and contribute new information on local environments. Finally, in Sec. V a quantitative analysis of the T_1 minima renders activation free energies which reflect important aspects of monolayer dynamics.

A. 0.2-layer data—a low-density gas and solidification

The transverse and longitudinal spin-relaxation times T_2 and T_1 for the lowest coverage CH_4 film taken at 4.586 MHz are shown in Fig. 7. We find the usual T_1 minimum associated with the correlation time $\tau \approx 1/\omega_L$ and the accompanying general decrease in T_2 with $1/T$ (Ref. 27). The T_2 values are down $1\frac{1}{2}$ orders of magnitude from the corresponding T_1 relaxation times which, as discussed in Sec. II A, is not unreasonable for lower-dimensional systems. The high-T side of the T_1 minimum appears to be nearly vertical at 55—57 K, although no break occurs in the T_2 data. In referring back to the phase diagram of Fig. 1, we see that a first-order solid-gas phase change does take place at 56 K. The T_1 minimum, then, sits well within the 2D "expanded" solid. Since for all coverages our data were only taken during warming, hysteresis was not studied. Likewise, insufficient low-temperature data prevent any appearance, in this or other coverages, of the expected 46-K solid-solid transition. The high-temperature gas-phase T_1 data has been least-squares fit with a $\sqrt{T}$ curve (heavy line through T_1 data for $T > 57$ K). This functional form was chosen because it is predicted for an ideal polyatomic gas with dipolar interactions (see Sec. II B). The fit is quite good over the high-T data and provides evidence that dipolar interactions are responsible for the T_1 relaxation process. We see no evidence for 2D liquefaction at any T.

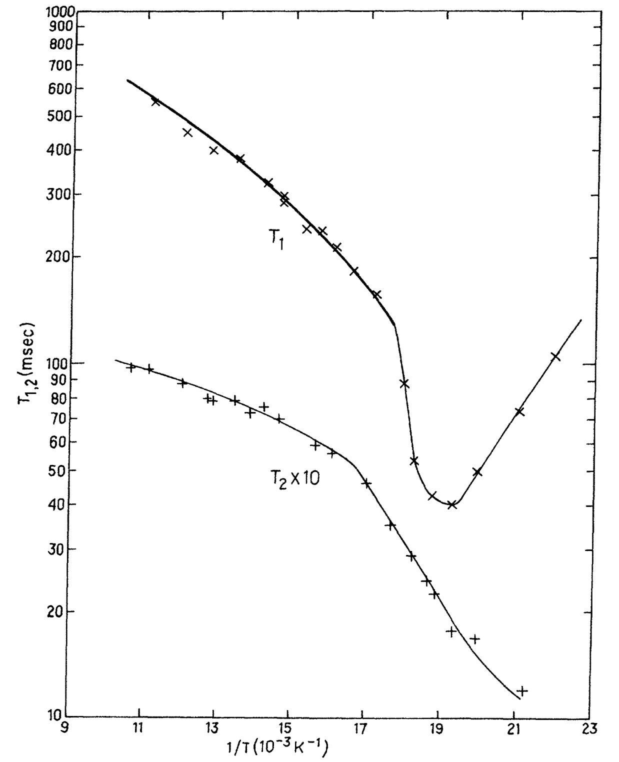

FIG. 7. 0.20-layer relaxation times. Heavy line is $\sqrt{T}$ fit. Other lines guide the eye.

One must be careful in analyzing low-coverage film measurements on Grafoil because surface heterogeneity effects can be sizeable.[28] The T_1 is sensitive to the time scale of adatom motion whereas T_2 is sensitive to the spread in local magnetic fields, with motion averaging these variations out. We therefore expect both T_1 and T_2 to change discontinuously when the mobility changes at the phase boundary, but we also expect T_2 to be more affected than T_1 by the heterogeneous region of the substrate. The short time drop in T_2 echo amplitudes mentioned previously suggests that bounded diffusion and boundary relaxation dominate T_2. The absence of a T_2 discontinuity at 56 K in the 0.2-layer data can therefore be understood as a heterogeneity effect.

Interestingly, T_2 rises no higher than about 10—15 msec for any mobile monolayer coverage. The T_2 for 2D gaslike helium films on Grafoil[29] likewise stayed below about 20 msec. It is reasonable to conclude that for comparable mobilities an adsorbate-independent T_2 limit is set by Grafoil field heterogeneities.[25,30] This intrinsic limit rounds all our T_2 curves somewhat.

B. 0.4—0.75 layers—solid, liquid, and hypercritical fluids

As the monolayer builds, we expect few changes in film behavior. Two-dimensional liquid droplets nucleate at various energetically favorable spots on the graphite.

These nuclei grow into puddles as coverage increases leaving the film local density fairly constant. When the temperature falls below 56 K, solidification of these droplets takes place. The NMR relaxation times shown in Fig. 8 appear quite similar to each other and to the 0.2-layer measurements. The T_1 minimum depths and temperatures remain stationary and their high-T sides still look discontinuous (although it is difficult to tell, since at 56 K T_1 is already changing rapidly). Fortunately, the low-coverage heterogeneity problem associated with our T_2 measurement has lessened, and a definite T_2 discontinuity now is evident at the liquid-solid phase boundary. We estimated the transition temperature for each coverage from the T_2 jump and placed these temperatures on a methane NMR phase diagram, □ in Fig. 9. It is difficult to estimate the temperature for the 0.7 and 0.75 data, because the jump decreases in size as coverage increases. It seems that the transition occurs near 57.5 K for these coverages and around 59 K for 0.4 and 0.6 monolayers. Error bars are the size of our symbols and temperatures are uncertain to ±1 K.

Some interesting structure is present in the T_1 data above about 60 K. There appears to be a coverage-*independent* rise just above melting, followed by a coverage *dependence* to the data at still higher T. In order to observe more carefully, we have plotted this T_1 data linearly versus temperature in Fig. 10. Straight line segments have been drawn through the data sets to approximate the two regimes. A slight shift of position for the steeper lines is probably associated with a similar shift in the position of the T_1 minimum with coverage. We have plotted the intersections of these line segments for the various coverages on our phase diagram, Fig. 9 (circles), with error bars as indicated. A smooth line has been drawn through these points which we interpret as the

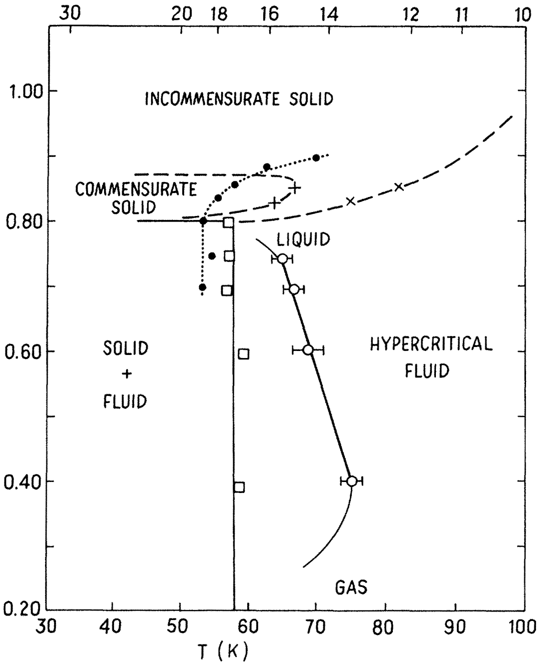

FIG. 9. T_1 vs temperatures in the fluid region.

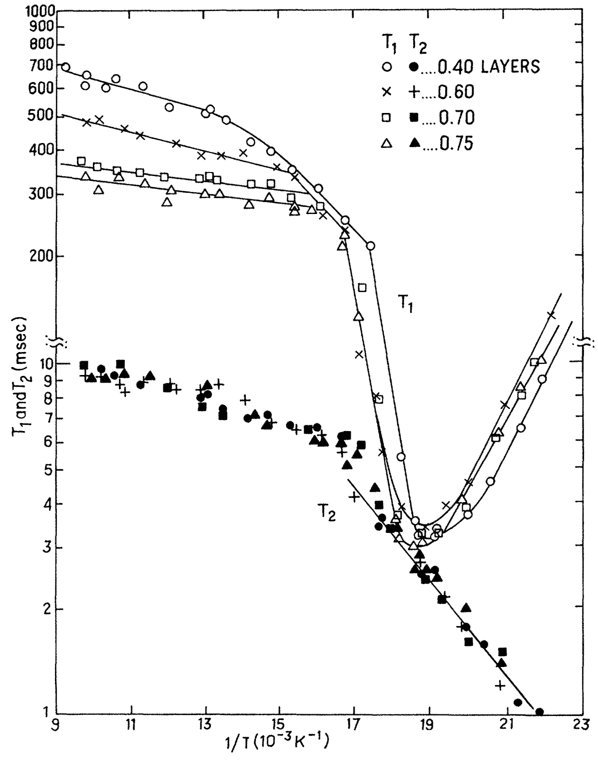

FIG. 8. (0.40—0.75)-layer relaxation time. Lines guide the eye.

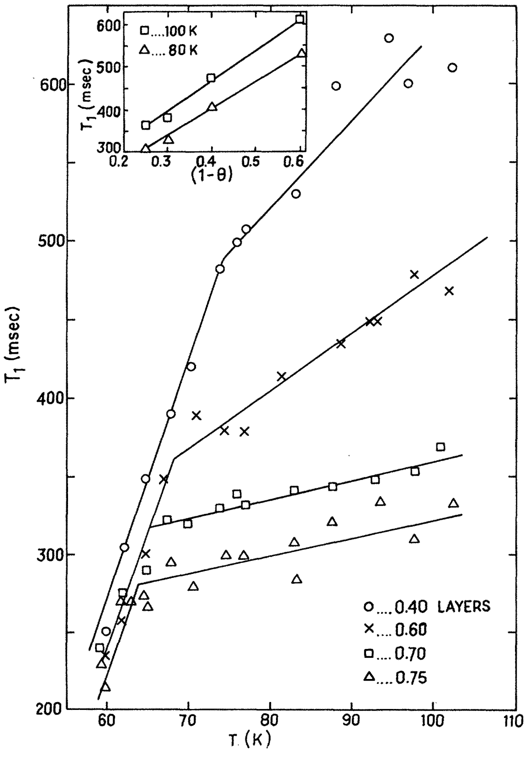

FIG. 10. (0.80—0.88)-layer relaxation times.

phase boundary between liquid and hypercritical fluid. As explained previously, the 0.2-layer data is gaslike, so our phase boundary drops sharply at low coverages.

This phase-boundary interpretation is supported by three arguments. First, Coulomb, Beinfait, and Thorel[6] have presented quasineutron scattering evidence for liquid and hypercritical fluid methane near the 2D critical point at 75 K. Second, the hypercritical fluid is a compressible nonideal gas, so a coverage dependence in the T_1 data is expected above 75 K but not in the two-phase region below the critical point. Finally, we can obtain diffusion coefficients D from our T_1 measurements for comparison with those of Coulomb *et al.* Assuming intramolecular relaxation and using Eqs. (2)—(4), $1/T_1=\gamma^4\hbar^2a^2/3b^6D$, where interproton distance $b=1.78\times10^{-8}$ cm, hard-core diameter $a=3.78\times10^{-8}$ cm, and $\gamma=2.67\times10^4$ rad/sec G gives $D=7.62\times10^{-5}T_1$. At 65 K, $T_1=300$ msec so $D=2.3\times10^{-5}$ cm^2/sec, which agrees with $D=2.6\pm0.3\times10^{-5}$ cm^2/sec for the two-phase-region fluid at 65 K obtained by Coulomb *et al.* (For a T_1 equal to 600 msec, $D=4.6\times10^{-5}$ cm^2/sec compared to their 13×10^{-5} cm^2/sec for $T=90$ K and 0.7 layers.) This agreement with previously measured diffusion coefficients shows consistency between the two experimental techniques, provides an explanation of our high-temperature T_1 drop with coverage, and further supports our model that the correlation times for the NMR signals is that for translational diffusion. Readers should be aware, however, that neither inelastic neutron scattering, Mössbauer experiments, nor T_1 measurements really measure D. They obtain τ_c and rely on dynamical modeling assumptions to relate τ_c to D. Field gradient NMR is required for a direct measurement of D. Such a measurement was actually performed for methane on Vulcan III, a graphitized carbon black by Tabony and Cosgrove.[31] They found $D=2.2$—2.7×10^{-5} cm^2/sec for 0.3—0.63 layer at 85 K, which falls well below the QENS high-T results. They do appreciate that Vulcan III is a poor-quality substrate and that heterogeneities cause much of the discrepancy. A molecular dynamics study[32] finds fluid diffusion constants which agree with the QENS measurements.

Notice that the T_1 slopes, or high-temperature apparent activation energies in Fig. 8, decrease with increasing coverage. This seems opposite to what one might expect since as the coverage is increased the mobility decreases and the activation energy should grow.

To explain this behavior we followed Coulomb *et al.*[6] in modeling the hypercritical fluid with the hole theory of liquids.[33] This theory postulates that the liquid exists in a lattice, but with many vacancies. The fluidity is proportional to the number of these "holes" and flows by molecules moving into them while expansion creates new holes. We obtained relaxation times from $T_1\approx D$ by a calculation of hopping frequencies (see Ref. 21 for details) and find $T_1\sim(1-\Theta)e^{\epsilon/kT}$ for intramolecular relaxation, where Θ is monolayer coverage. If the dominant relaxation mechanism were intermolecular instead then $T_1\sim(1-\Theta)/\Theta$, since $T_1\sim D/\rho$. Our high-temperature T_1 data, when plotted as $1-\Theta$, is clearly linear (inset of Fig. 10).

C. 0.80—0.88 layers—commensurate solid, intermediate phase, and fluid

This coverage range is the most interesting part of the monolayer phase diagrams. The film fills the entire graphite basal surface and further adsorbed methane molecules increase the chemical potential to the place where film compression, new relaxation mechanisms and additional phases must be considered. The T_1 data of Fig. 11 is richer in detail than lower coverage results. At 0.80 layers the high-temperature side of the T_1 minimum has broadened, signifying that the first-order phase transition is weakening. Confirmation comes from the T_2 data, which can still be approximated by two straight line segments whose intersection (also plotted in Fig. 9) agrees with the T_1 fall off. This feature disappears at higher coverages.

The T_1 minimum broadens and shifts to higher temperatures as coverage further increases. This reflects a change in the relation between correlation time τ_c and temperature. Since $\omega\tau_c=0.62$ at the T_1 minimum, additional thermal activity is required to maintain optimal spin-lattice relaxation in these dynamically congested films. The locus of the T_1 minima appears on the phase diagram as a dotted line. A temperature shift commences at 0.80 layers where, from the neutron scattering phase di-

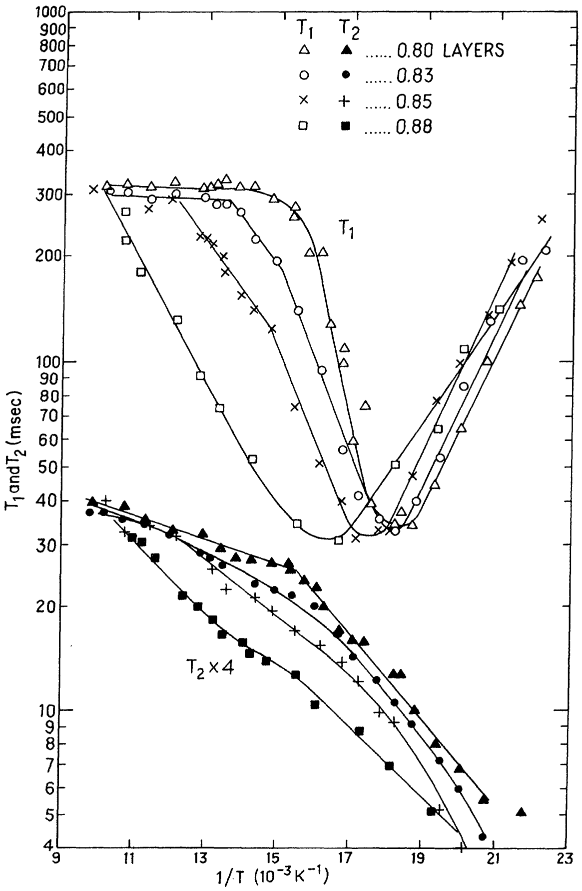

FIG. 11. (0.88—1.10)-layer relaxation times.

agram, we know that the single-phase 2D solid first appears.

A new and intriguing T_1 feature becomes increasingly dominant as coverage increases from 0.83 to 0.88 layers. An intermediate phase evidently exists with a distinctly lower T_1 slope, and therefore lower activation energy, than the film possesses at temperatures near the T_1 minimum. The positions of the slope discontinuities are added to the phase diagram ($+$, $\times$ in Fig. 9) and suggested phase lines are dashed in. The high-T line corresponds closely to the expanded solid-fluid boundary of Fig. 1. We delete the solid-plus-fluid high-temperature "sliver" since no NMR or neutron scattering evidence for this feature has been found. Furthermore, our transition appears to be continuous (no T_1 discontinuity) making an excluded region of the phase diagram unnecessary. Thomy, Duval, and Regnier[34] do report an isotherm riser here, but not the clear discontinuity expected of a two-phase region. Our lower T-phase line was not specified by neutron scattering. We believe that the 50-K commensurate solid—expanded-solid phase boundary was incorrectly placed on their phase diagram due to considerable data scatter in this region. We feel that those measurements are consistent with a phase boundary reaching 68 K and therefore label the lower temperature phase as commensurate solid. The intermediate-temperature phase would correspond to an expanded solid with melting at still higher T. As coverage increases to 0.88 layers the commensurate solid appears to disappear completely with no sharp low-T feature at all in the now quite broadened T_1 data. The commensurate phase, then, is displaced at *both* higher temperature and higher coverage by another more stable phase. The phase lines in this near-monolayer regime are shown as dashed since no NMR evidence exists for discontinuities (although Neilsen *et al.*[35] do see a first-order transition at very low T on *ZYX* graphite).

We mentioned that the 0.80-layer T_2 data has a break in slope at 0.0155 K^{-1}. At higher coverages the T_2 acquires a more gradual change of slope which occurs in the intermediate-phase region. T_2 does not show the detail of the T_1 data, because it is dominated by boundary relaxation effects.

D. 0.90—1.10 layers—compressed solid

The T_2 data here is steep but featureless and the T_1 minimum rapidly shifts to higher temperature with increasing coverage (Fig. 12). The T_1 minimum narrows appreciably at monolayer completion where the highest density occurs. No phase-transition features are apparent in the T_1 data.

It is instructive to plot T_2 versus coverage at constant temperature. We have done so at 10-K intervals from 50 to 90 in Fig. 13. At low temperatures (T=50 K) T_2 remains constant until 0.80 monolayers, then falls somewhat as mobility decreases upon entering the one-phase commensurate solid. For higher temperatures the drop is quite dramatic as one crosses the liquid-solid boundary between 0.8 and 0.9 layers. As coverage is further increased, we observe a leveling out of T_2, indicating that the monolayer and second-layer methane adatoms are not very

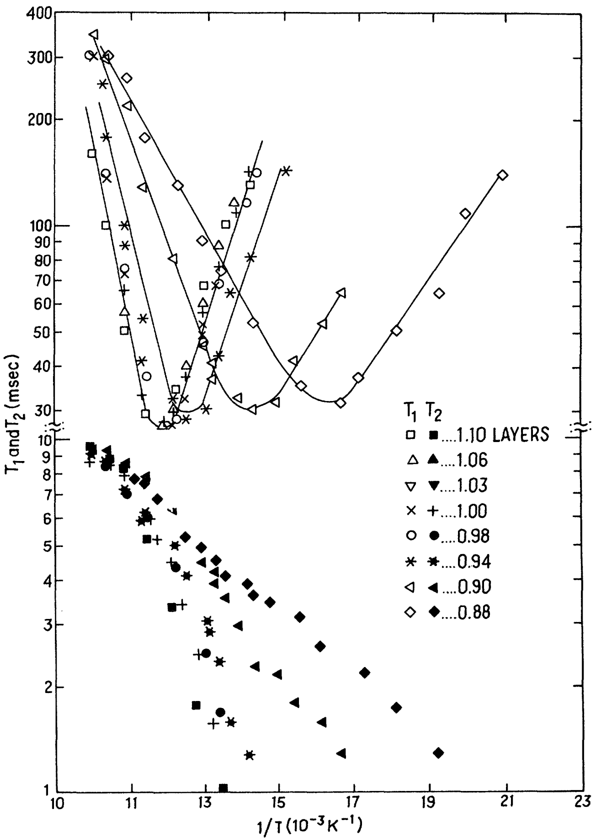

FIG. 12. NMR methane phase diagram. Solid lines, first-order transitions; dashed lines, continuous transitions; dotted line and solid dots, locus of the T_1 minimum. Symbols are explained in text.

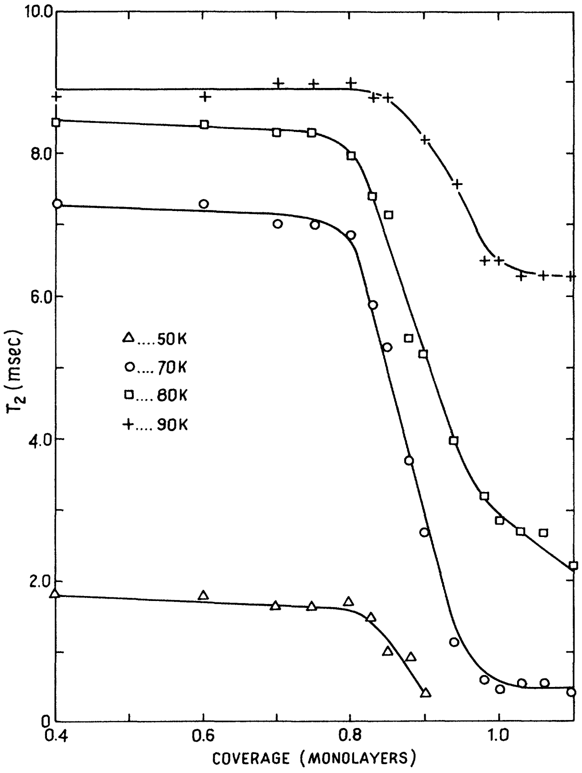

FIG. 13. T_2 vs coverage.

mobile. (A similar plot for ^{3}He films shows that motional narrowing again increases T_2 beyond monolayer completion.[29])

E. $CH_4 + CD_4$ mixtures

These experiments measured the proton relaxation times in a 50% mixture of CH_4 and CD_4. Data were taken at the three total ($CH_4 + CD_4$) coverages of 0.70, 0.85, and 0.94 monolayers so as to intersect the major regions of the phase diagram. Because the deuterium nucleus has a magnetic moment one-third that of the proton, the proton-deuteron intermolecular dipolar interaction will be reduced from the proton-proton dipolar strengths by the factor

$$\alpha=\tfrac{2}{3}(\gamma_D/\gamma_P)^2 I_D(I_D+1)/I_P(I_P+1)\ ,$$

where $\gamma_D/\gamma_P=0.154$, $I_D=1$ and $I_P=\frac{1}{2}$, giving $\alpha=0.042$ (Ref. 16, p. 328). A 50% mixture of CH_4 and CD_4 should then double the relaxation times if intermolecular dipolar interactions were dominant (half the molecules have 0.042 times the interaction strength), and have no effect if intramolecular interactions prevail.

The results for 0.70, 0.85, and 0.94 monolayers, found in Figs. 14, 15, and 16, respectively, show a striking feature. Although the T_2 values are only slightly lower than the pure film data, the T_1 minima at these near monolayer coverages have *broadened* and *shallowed* dramatically. In addition, the liquid relaxation times of the mixture are substantially lower than those of the pure liquid. This effect cannot be explained by simply saying that the activation energy, which is determined by the slope of the T_1 data has decreased while the value of T_1 at the minimum has increased due to smaller intermolecular interactions. That would be saying that the correlation times that are related to temperature by $\tau_c=\tau_0 e^{\epsilon/kT}$ have changed substantially. But we know that $\tau_c=0.62/\omega_L$ at the T_1 minimum and the minimum remains fixed in T

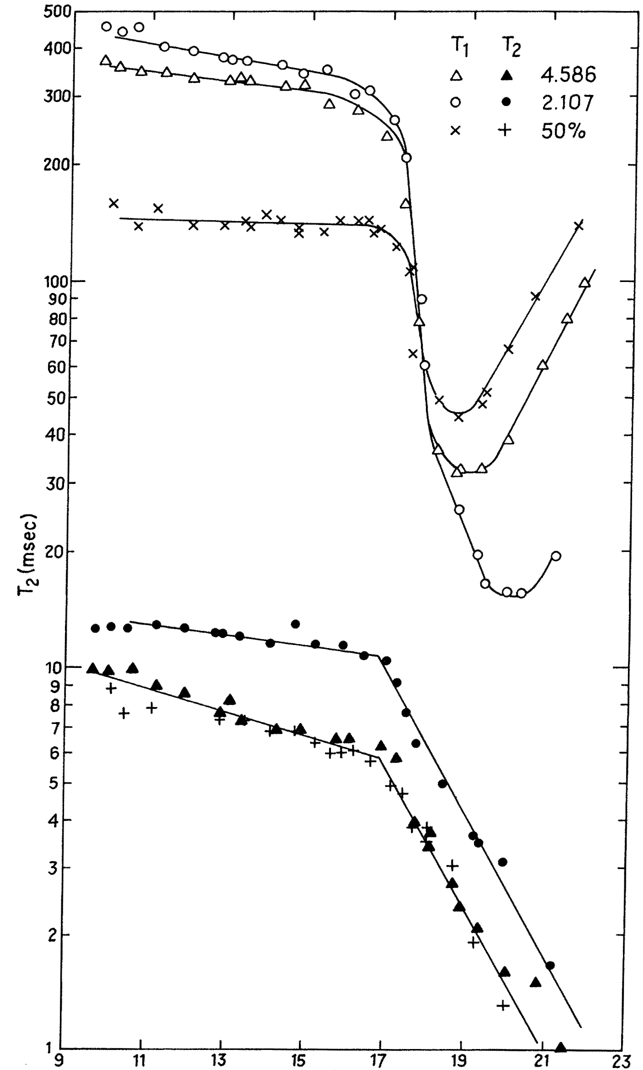

FIG. 14. 0.70-layer mixture and low-frequency data.

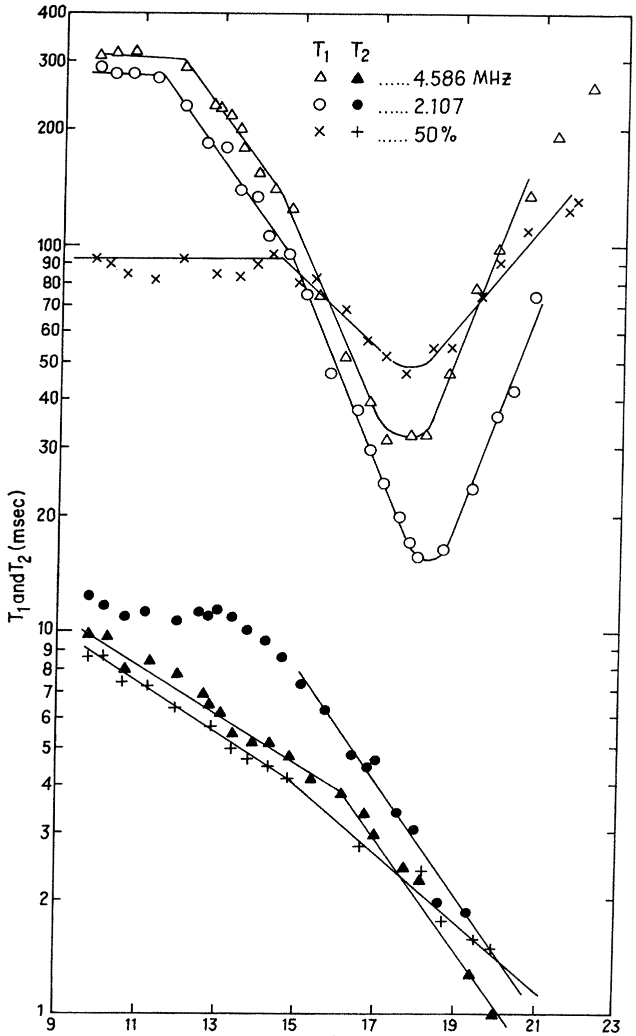

FIG. 15. 0.85-layer mixture and low-frequency data.

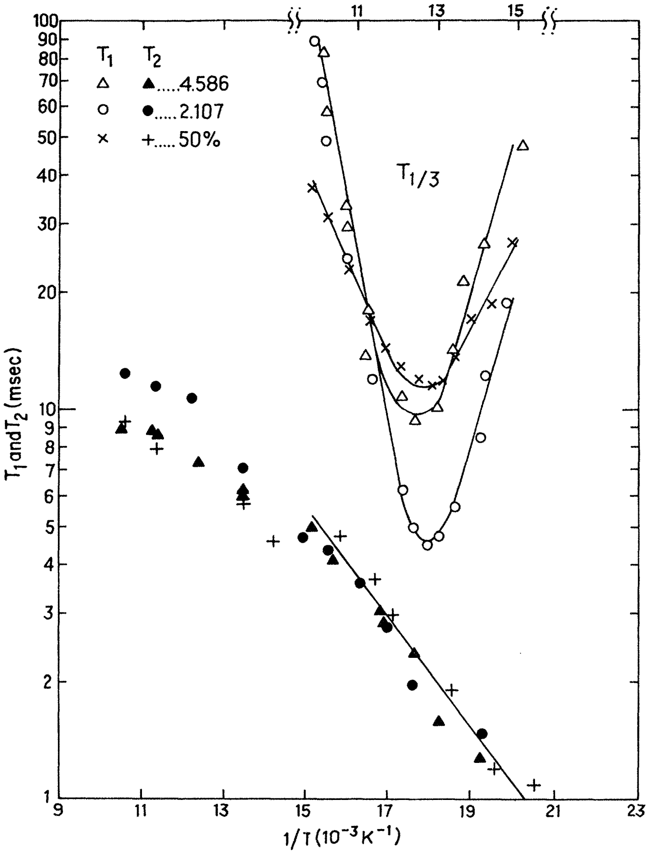

FIG. 16. 0.94-layer mixture and low-frequency data.

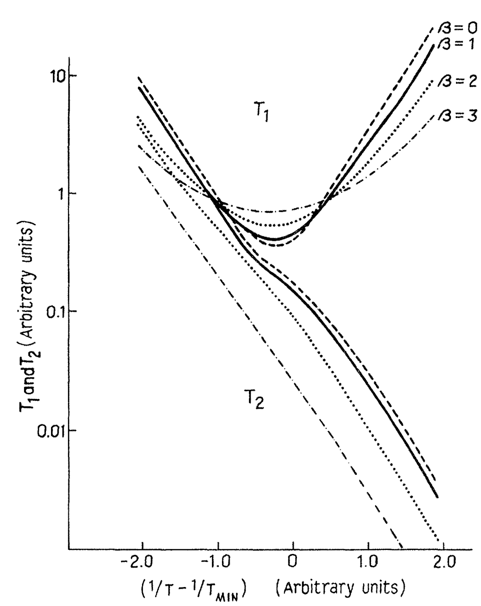

FIG. 17. Effects of spread in activation energies. Parameter β is explained in text (from Ref. 37).

with deuteration. In addition, the value of T_1 at the minimum has not doubled, but has only increased by 40—50 % upon deuteration.

Work done by Nowick *et al.*[36] have shown just such an effect. If one assumes a distribution in correlation times about a mean, where $p(\tau)$ is the normalized distribution function, and fast exchange exists between the regions of varying τ (which is the case in this experiment), then

$$\frac{1}{T_1}=\int_0^\infty p(\tau_c)\frac{1}{T_1(\tau_c)}\ .$$

With the use of the Arrhenius activation energy law, $\tau_c=\tau_0 e^{\epsilon/kT}$, this could mean a variation in the attempt frequency, $1/\tau_0$, and/or in the activation energy ϵ. Both of these variations are present. They evidently arise from local density and thermal activity variations caused by the considerable mass difference (25%) of the two methanes.

Assuming a log-normal distribution of correlation times, i.e., a Gaussian spread in activation energy with a width $\beta=\sqrt{2}(E_c-\langle E_c\rangle/2kT)^2$, the shape of the curve $\ln(T_1)$ vs $\omega\tau_c$ can be calculated.[36] The results for different values of β are plotted in Fig. 17.[37] Notice not only the *apparent* decrease in activation energy, but the rise in the value of the T_1 minimum and slight decrease in T_2. Calculations using different distribution functions[38] produce similar results. One can compute β by estimating the width at half minimum and the rise in the T_1 minimum. Each of these measurements for all coverages independently gives $\beta\cong 1.5$. In particular, the total increase in the value of the observed T_1 minimum is consistent with only a spread in activation energy and *not* with a decrease in dipolar coupling. The CD^4 T_1 data therefore supports the assumption of intramolecular relaxation.

The spread in correlation times evidently also occurs for the liquid phase where T_1 is lowered, but since $\omega_L\tau_c \ll 1$ there is not a minimum. A strong inflection point in the 0.85-layer CD_4 data is present at the commensurate-incommensurate phase transition, further highlighting this important transition. It might be thought that activation energy changes in the pure-CH_4 data are due to spreads in activation energy as well. However, the activation energy can also be obtained from the shifts in the T_1 minima of the 2-MHz data (Figs. 14—16). These values corroborate our interpretations. The T_2 data are also frequency sensitive, but this merely reflects a modified sampling of Grafoil local-field heterogeneities.

V. THE T_1 MINIMUM—A QUANTITATIVE ANALYSIS

A. Position and depth of the T_1 minimum

The region of the T_1 minimum contains quantitative information which can be obtained through analysis of changes in its depth, position, and width with coverage. In Fig. 18(a) we have given for inverse temperatures, the main phase-diagram features of Fig. 9. The locus of the T_1 minimum (solid circles) remains wholly within the solid monolayer phases. A weak temperature shift is apparent in the two-phase region below 0.8 layers. Upon entering the single-phase-ordered solid, the T_1 minimum rises dramatically toward much higher temperatures, pass-

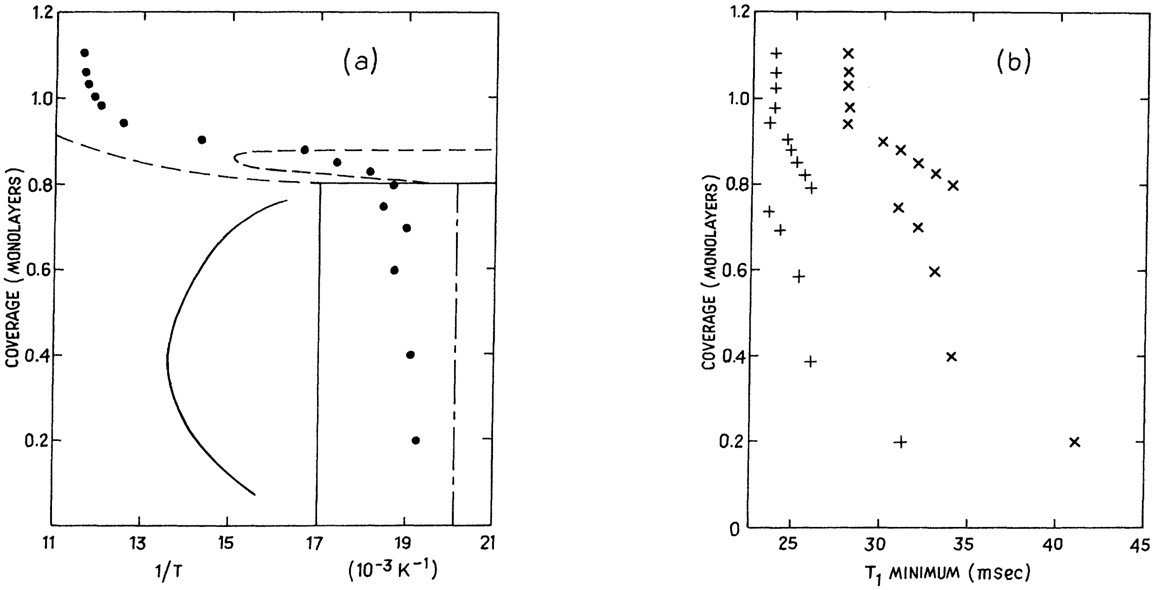

FIG. 18. (a) Temperature of the T_1 minimum vs coverage. Solid and dashed lines are phase diagram features from Fig. 12. (b) Depth of T_1 minimum vs coverage. $\times$, depth; $+$, depth corrected for spin-species effects.

ing through the 0.88-layer commensurate-incommensurate transition (CIT) without incident before stabilizing again above monolayer completion. Its temperature dependence tells us that as coverage increases beyond 0.8 layers, greater molecular activity provided by the higher temperatures is required to maintain a constant correlation time (since at the minimum $\tau_c \omega_L = 0.62$). This increased thermal activity counteracts the decreased molecular mobility due to compressional effects within the incommensurate solid near monolayer completion.

The accompanying diagram shows how the T_1 minimum depth changes with coverage [$\times$'s in Fig. 18(b)]. There is about a 5-msec (20%) variation of the minimum from 0.4 to 1.1 layers with an apparent discontinuous change at the 0.8-layer phase boundary. (The 0.2-layer point is anomalously high. We believe that heterogeneities are to blame.) The coverage dependence of the minimum temperature [Fig. 18(a)] appears to reflect density variations within the different monolayer phases. However, intramolecular relaxation processes should be *in*sensitive to the film density so we expect that the T_1 minimum *depth* [Fig. 18(b)] would be a constant, independent of coverage.

As explained in the Appendix, intramolecular dipolar interactions arise from a combination of separate interactions involving the various spin species of methane. The relative fraction of species present is temperature dependent and affects the measured T_1 values. In particular, corrections to the T_1 minimum depth of Fig. 18(b) can be made from a knowledge of the temperature of the T_1 minimum as given in Fig. 18(a). Data points are corrected using Eq. (A1) with $X(\tau)$ values as determined from Fig. 21. The corrected data [$+$ in Fig. 18(b)] now appears about constant at 24 msec/$X(\infty)$, where in the high-T limit, $X(\infty)=1.63$. Although the discontinuity at 0.80 layers remains, it amounts to only a few msec jump and is within the 10% resolution of our T_1 data. Numerical comparison with these T_1 minimum relaxation times using Eq. (2.3) are subject to formulation assumptions. Sprik and Trappeniers[39] find $T_{1_{\min}}^{\text{intra}} \sim 16$ msec for orientationally ordered molecules of a powder. This is quite close to our observation although determinations of the proportionality constant [$\frac{2}{5}$ in Eq. (2.3)] are not completely consistent in the literature.[40]

B. T_1 and T_2 activation energies

Activation energies were computed by fitting Eq. (2.3) for two-proton intramolecular relaxation

$$\frac{1}{T_1}=\frac{2}{5}\frac{\gamma^4\hbar^2}{b_6}I(I+1)\left[\frac{\tau_c}{1+\omega^2\tau_c^2}+\frac{4\tau_c}{1+4\omega^2\tau_c^2}\right]$$

to the T_1 curves. The prefactor was determined empirically by substituting T_1 into the equation at $\omega\tau_c \cong 0.62$, the T_1 minimum. The τ_c's for other values of T_1 were computed by Newton's method for finding roots of an equation and then fit to the Arrhenius equation $\tau_c = \tau_0 e^{\epsilon/kT}$, the temperatures for each $\tau_c(T_1)$ being known. Even though the methane molecule contains four protons not two, this equation gave a good fit to the data, especially near the minimum where the fit is very sensitive to the form of the equation. Use of only one term in Eq. (2.3) significantly reduces the quality of the fit, and adding a third term does not improve it. When a T_1 minimum was absent (because $\omega\tau_c \ll 1$) activation energies were calculated by fitting $\ln(T_1)$ vs $1/T$ to a straight line, since T_1^{-1} becomes proportional to τ_c. A T_2 activation energy analysis will *not* be presented since it is understood that in lower-dimensional systems T_2 is not simply

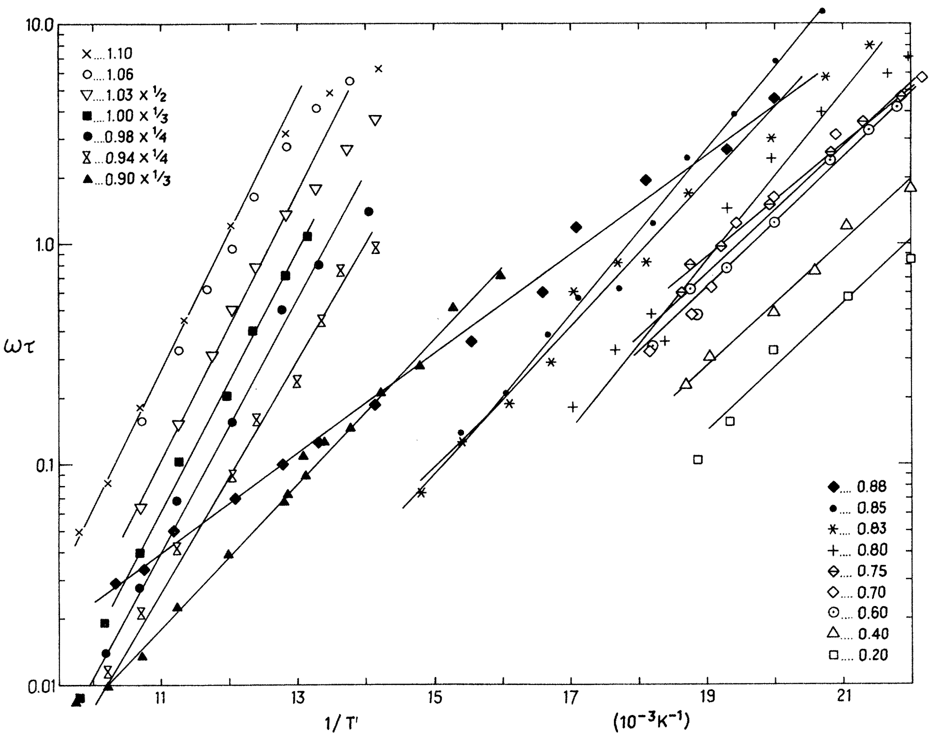

FIG. 19. Arrhenius plot of all T_1 data. Least-squares fits are shown for each data set.

related to τ_c, rendering an Arrhenius plot meaningless.[13] Spin-species corrections to ϵ are of second order since $\log(X)$ has a weak T dependence.

In Fig. 19 we have provided a compilation of all our processed T_1 data along with a least-squares linear fit for each coverage. The slope and $1/T=0$ intercepts of these fits give T_1 activation energies and τ_0's, respectively. The resulting ϵ's obtained from the T_1 analysis are shown in Fig. 20. Error bars are 2σ of the linear least-squares fit to the T_1 relaxation data. We do not show or tabulate τ_0's because extrapolation uncertainties are so great. It should be mentioned, however, that these values are directly related to attempt entropies Δs through the activation free energy since $\tau_0 \propto e^{(\epsilon - T\Delta s)/kT}$. The values of $\Delta s/k$ are quite large ($\sim$3.5 per activation).

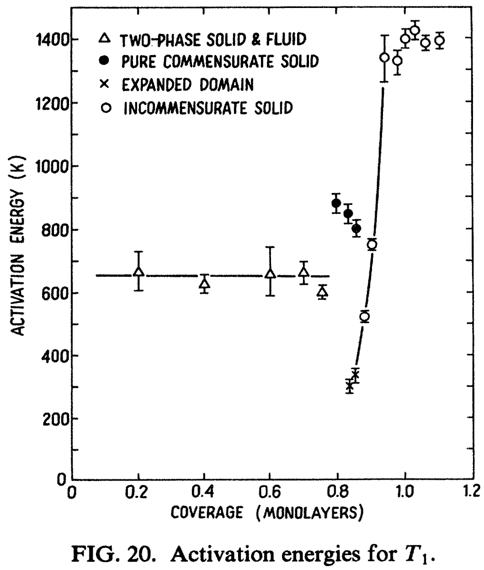

FIG. 20. Activation energies for T_1.

C. Activation mechanisms and misfit dislocations

Now we can see clearly that different regions of the phase diagram possess distinctly different ϵ's and therefore unique activation mechanisms. From Fig. 20 we observed a nearly constant ϵ of 650 K for low coverages where solid and fluid coexist (error bars are 1-standard-deviation uncertainties). By 0.80 layers the 2D solid islands merge and ϵ increases abruptly, signaling a new activation mechanism: Voids, interstitials, and other defects rearrange themselves. With increasing coverage across the commensurate phase, ϵ decreases as the spreading pressure grows. Activation energies for the higher T expanded domain are included in the figure. They are *much* lower than the ϵ's for the commensurate phase but are comparable to the activation energy of the compressed solid at 0.88 layers. The precipitous fall and smooth progression of ϵ between 0.83 and 0.94 layers convince us that the expanded domain and compressed phase are actually a *single* incommensurate phase bounding the commensurate solid. On nearing monolayer completion, activation processes are inhibited by compression and the ϵ rises even further to 1400 K where it finally stabilizes with second-layer formation.

To estimate the relative strengths of activation barriers, some simple modeling calculations were performed.[14] The energy required for 2D evaporation from the edge of a solid island was found to be $\sim$300 K per molecule and the energy for moving into a vacancy was determined as $\sim$450 K. The ratio of these values is consistent with our ϵ ratio from the two phase and commensurate solid phase. More rigorous calculations for methane monolayers were made by Phillips and Hammerbacher.[41] They find the molecular interaction potential for $\sqrt{3}$ packing to be 914 K and a 2577-K heat of desorption from the commensurate phase. We measure a (800—900)-K activation energy in the $\sqrt{3}$ phase and find that the compressed monolayer's $\epsilon \simeq 1400$ K is only marginally less than the 1609 K observed for bulk solid methane.[42] A simulation study of near monolayer methane phases has recently been performed.[43]

The actual dynamic mode(s) which determine(s) the activation free energy changes on passing through the CIT cannot be specified from our NMR data alone. Several possible 2D mechanisms have recently been discussed in the literature. Among these are domain wall unpinning,[44] dislocation dynamics,[45] and grain-boundary generation.[46] Our activation energies and CIT phase-diagram features do correspond reasonably well to the predictions of Frank and Van der Merwe (FVdM model) for misfit dislocations.

DVdM (Ref. 47) investigated the potential energy competition between a chain of molecules with spring constant μ and periodicity b, with the underlying substrate lattice having strength $W/2$ and periodicity a, and showed that 2D films could be analyzed using this 1D model. The ratio l_0/P_0 determines the system's behavior, where the parameter $l_0=(\mu a^2/2W)^{1/2}$ measures domain wall width and $P_0=b/(a-b)$ is the vernier period of misfit. If $l_0/P_0<2/\pi=0.64$, registry occurs and a large ϵ is required to unpin dislocations. However, as l_0/P_0 crosses $2/\pi$ with increasing coverage, dislocation formation is favored, ϵ drops drastically and a CIT results. Applying the FVdM equation with CH_4-graphite Lennard-Jones parameters of $\epsilon=148.9$ K and $\sigma=3.78$ Å (Ref. 32) (for a molecular dynamics modeling treatment see Ref. 43) $W=11$ K,[41] $a=4.26$ Å, and $b=4.19$ Å (Ref. 1) gives $\mu=946$ K/Å, $l_0=27.9$, $P_0=60.9$, and $l_0/P_0=0.459$.[14] Thus a commensurate region capable of enduring a $2/\pi l_0=2.3\%$ misfit is predicted. This would place the zero misfit monolayer at 0.87—0.023=0.85 actual layers. The FVdM activation energy here is $\sim$700 K,[14] in agreement with our $\epsilon=800$ K. The calculated ϵ at critical misfit drops to 125 K, even lower than our observations, showing that dislocation unpinning is a probable activation mechanism.

ACKNOWLEDGMENTS

We wish to thank M. G. Richards, N. S. Sullivan, R. Clarke, and J. R. Brookeman for valuable discussions of the data and I. Ward and L. Thurston for help on the manuscript. One of us (M.B.) appreciates the hospitality extended by A. L. Thomson while at Sussex University during part of this work. Support was provided by the National Science Foundation (Grant No. DMR-79-03614) and by a University of Michigan Phoenix Memorial Grant. It is based on the thesis work of one of us (J.H.Q.).

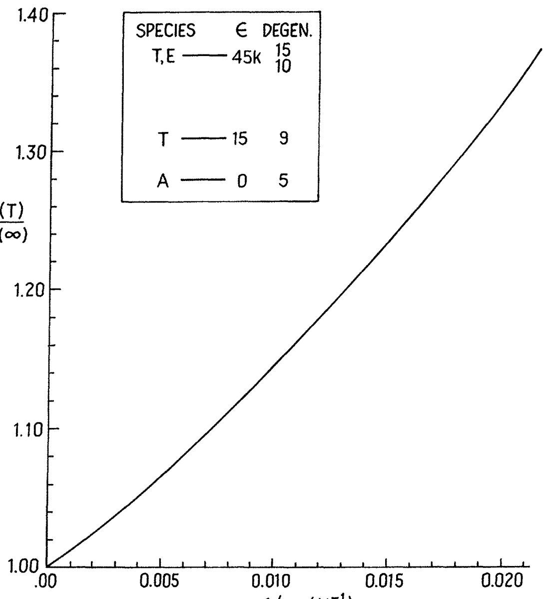

FIG. 21. Spin temperature corrections. Inset: Energy level diagram for methane spin species.

APPENDIX A: SPIN RELAXATION MECHANISMS

We have presented considerable experimental evidence that the spin-lattice relaxation time T_1 for methane adsorbed on graphite is determined by intramolecular dipolar interactions. In analyzing these relaxation times quantitatively, one must realize that there are different intramolecular interactions for the various molecular spin species I_{total} of methane. The A, T, and E species, representing different irreducible tetrahedral groups, correspond to orbital wave functions with $I_{\text{total}}=2$, 1, and 0, respectively. The species are expected to communicate rapidly within the Grafoil at high temperatures thereby maintaining thermal equilibrium between the different energy levels. These libron levels, shown in the inset of Fig. 21, have been measured for the 3D gas by Briganti.[48] The lowest-lying A level has a degeneracy of $g_A=5$, while the first excited level is a T state at 15 K with $g_T=9$. The second level at 45 K is shared by T and E states where degeneracies are $g_T'=15$ and $g_E=10$. (These levels are a bit higher than those calculated for solid methane.)

The relative population between these levels is, of course, temperature dependent. For intramolecular interactions only the T species has nonzero matrix elements giving rise to relaxation. The A and E species have symmetric wave functions, and so they do not contribute directly, but they do relax via the T state which tends to lengthen the observed T_1 relaxation times, $T_1\,|_{\text{expt}}$,[42]

$$T_1\,|_{\text{expt}}=\chi(T)T_1\,|_{(T\text{ species})}\ . \tag{A1}$$

We can obtain an estimate of the temperature dependence of $T_1\,|_{\text{expt}}$ through the function

$$\chi(T)=\frac{\sum_i g_i I_i(I_i+1)N_i}{g_T I_T(I_T+1)N_T}=\frac{2N_T+6N_A}{2N_T}\,,\quad i=A,T,E$$

which weights the thermal content of the three species.

Assuming that the level populations are proportional to their Boltzmann factors (i.e., thermal equilibrium), we have

$$\frac{N_A}{N_T}=\left[\frac{Ng_A e^{-\epsilon_A/kT}}{\sum_i e^{-\epsilon_i/kT}}\right]\Bigg/\left[\frac{N(e^{-\epsilon_T/kT}+e^{-\epsilon'_T/kT})}{\sum_i e^{-\epsilon_i/kT}}\right]$$

$$=\frac{g_A e^{-\epsilon_A/kT}}{g_T e^{-\epsilon_T/kT}+g'_T e^{-\epsilon'_T/kT}} .$$

For $\epsilon_A=0$, $\epsilon_T/k=15$ K, $\epsilon'_T/k=45$ K, and the g's given previously,

$$\chi(T)=1+\frac{1}{0.6e^{-12.7T}+e^{-45.2/T}} . \tag{A2}$$

This function, plotted versus temperature in Fig. 21, is used in the main text to estimate corrections to the T_1 minima. The deviation of $\chi(T)$ from its high-T limit, $\chi(\infty)=1.63$, is only modest in the temperature range of the present experiment.

---

[*] Present address: Francis Bitter National Magnet Laboratory, Massachusetts Institute of Technology, Cambridge, MA 02139.

[1] C. Tessier and Y. Larher, in *Ordering in Two Dimensions,* edited by S. K. Sinha (North-Holland, Amsterdam, 1980), p. 163.

[2] P. Vora, S. K. Sinha, and R. K. Crawford, Phys. Rev. Lett. 43, 704 (1979).

[3] P. Dutta, S. K. Sinha, P. Vora, M. Nielsen, L. Passell, and M. Bretz, in *Ordering in Two Dimensions,* edited by S. K. Sinha (North-Amsterdam, Holland, 1980), p. 169.

[4] S. K. Sinha, P. Vora, P. Dutta, M. Nielsen, and M. Bretz (unpublished).

[5] A. Glauchant, J. P. Coulomb, and M. Bienfait, and J. G. Dash, J. Phys. (Paris) Lett. 40, L543 (1979); A. Glauchant, J. P. Coulomb, M. Biefait, P. Thorel, C. Marti, and J. G. Dash, in *Ordering in Two Dimensions,* edited by S. K. Sinha (North-Holland, Amsterdam, 1980), p. 203.

[6] J. P. Coulomb, M. Bienfait, and P. Thorel, in 2D Adsorbed Phases, edited by M. Bienfait and J. Suzanne [J. Phys. (Paris) Colloq. 38, C4-31 (1977)]; Phys. Rev. Lett. 42, 733 (1979); J. Phys. (Paris) 42, 293 (1981).

[7] A. Thomy and X. Duval, J. Chem. Phys. 66, 1966 (1969); 67, 1101 (1970).

[8] P. Thorel, J. P. Coulomb, and M. Bienfait, Surf. Sci. Lett. 114, 143 (1982).

[9] M. W. Newbery, T. Rayment, M. U. Smalley, R. K. Thomas, and J. W. White, Chem. Phys. Lett. 59, 461 (1978).

[10] R. Marx and E. F. Wassermann, Solid State Commun. 40, 959 (1981); Surf. Sci. 117, 267 (1982).

[11] A. D. Migone, M. W. H. Chan, and J. R. Boyer, Physica 108B, 787 (1981).

[12] J. W. Riehl and K. Koch, J. Chem. Phys. 57, 2199 (1972).

[13] B. P. Cowan, J. Phys. C 13, 4575 (1980); J. Low Temp. Phys. 50, 135 (1983).

[14] J. H. Quateman and M. Bretz, Phys. Rev. Lett. 49, 1503 (1982).

[15] T. Farrar and E. Becker, *Pulse and Fourier Transform NMR* (Academic, New York, 1971).

[16] A. Abragam, *The Principles of Nuclear Magnetism* (Oxford University Press, New York, 1961).

[17] R. Kubo, J. Phys. Soc. Jpn. 9, 888 (1954); 17, 1100 (1962).

[18] A. Landesman, Ann. Phys. (Paris). 8, 53 (1973).

[19] M. Bloom, F. Bridges, and W. Hardy, Can. J. Phys. 45, 3533 (1967).

[20] D. F. Holcomb and R. E. Norberg, Phys. Rev. 98, 1074 (1955).

[21] J. H. Quateman, Ph.D. thesis, University of Michigan, 1982 (unpublished).

[22] W. G. Clark and J. A. McNeil, Rev. Sci. Instrum. 44, 844 (1973).

[23] G. I. Rochlin, Rev. Sci. Instrum. 41, 73 (1970).

[24] J. G. Dash, *Films on Solid Surfaces* (Academic, New York, 1975).

[25] M. G. Richards (private communication).

[26] L. J. Friedman, P. J. Millet, and R. C. Richardson, Phys. Rev. Lett. 47, 1078 (1981).

[27] N. Bloembergen, E. M. Purcell, and R. V. Pound, Phys. Rev. 73, 679 (1948).

[28] R. L. Elgin, J. M. Greif, and D. L. Goodstein, Phys. Rev. Lett. 41, 1723 (1978).

[29] J. Owers-Bradley, Ph.D. thesis, University of Sussex, 1978 (unpublished).

[30] D. L. Husa, D. C. Hickernel, and J. E. Piott, in *Monolayer and Submonolayer Helium Films,* edited by J. G. Daunt and E. Levner (Plenum, New York, 1973), p. 133.

[31] J. Tabony and T. Cosgrove, Chem. Phys. Lett. 67, 103 (1979).

[32] S. Toxvaerd, Phys. Rev. Lett. 43, 529 (1979).

[33] S. Glasstone, K. J. Laidler, and H. Eyring, *Theory of Rate Processes* (McGraw-Hill, New York, 1941).

[34] A. Thomy, X. Duval, and J. Regnier, Surf. Sci. Rep. 1, 1 (1981).

[35] M. Nielsen, J. Als-Nielsen, and J. P. McTague, in *Ordering in Two Dimensions,* edited by S. K. Sinha (North-Holland, Amsterdam, 1980), p. 139.

[36] A. S. Nowick and B. S. Berry, IBM J. Res. Dev. 5, 297 (1961).

[37] H. Pfeifer, NMR Basic Principles and Progress 7, 53 (1972). 51, (12), 5673 (1969).

[38] F. Noack and G. Preissing, Z. Naturforsch 24A, 143 (1969).

[39] M. Sprik and N. J. Trappeniers, Physica 103A, 411 (1980).

[40] N. S. Sullivan (private communication).

[41] J. M. Phillips and M D Hammerbacher, Bull. Am. Phys. Soc. 27, 309 (1982).

[42] G. A. Dewit and M. Bloom, Can. J. Phys. 43, 986 (1965).

[43] E. S. Severin and D. J. Tildesley, Mol. Phys. 41, 1401 (1980) and unpublished.

[44] V. L. Pokrovskii, J. Phys. (Paris) 42, 761 (1981).

[45] G. Schock, in *Dislocations in Solids,* edited by F. R. N. Nabarro (North-Holland, Amsterdam, 1980), Vol. 3, p. 63.

[46] S. T. Chui, Phys. Rev. Lett. 48, 933 (1982).

[47] F. C. Frank, and J. H. Van der Merwe, R. Proc. Soc. London 198, 205 (1949).

[48] G. Briganti, P. Calvani, F. DeLuca, and B. Maraviglia, Can. J. Phys. 56, 1182 (1978).